Supporting Information

Electron-transfer enhanced of urchin-like CoP-$Ce_2(CO_3)_2O$/NF as ultra-stable bifunctional catalyst for efficient overall water splitting

Lixia Wang [a], Meilin Huang [a], Mingcheng Gao [a], Tayirjan Taylor Isimjan [b] *, Xiulin Yang [a] *

[a] *Guangxi Key Laboratory of Low Carbon Energy Materials, School of Chemistry and Pharmaceutical Sciences, Guangxi Normal University, Guilin 541004, China*

[b] *Saudi Arabia Basic Industries Corporation (SABIC) at King Abdullah University of Science and Technology (KAUST), Thuwal 23955-6900, Saudi Arabia*

E-mail: xlyang@gxnu.edu.cn; isimjant@sabic.com

Materials characterization

The composition of all sample was ascertained by X-ray diffraction X-ray diffraction (XRD, Rigaku D/Max-3c) using a D/Max 2500 V PC with Cu Kα radiation (Rigaku, USA). The scanning electron microscopy (SEM, Quanta FEG 200, Holland) and transmission electron microscopy (TEM, Talos F200S) were employed to analyze the morphology of electrocatalysts. The energy-dispersive X-ray (EDX) spectroscopy was carried out to examine the composition. X-ray photoelectron spectroscopy was carried out to examine the materials' elemental and surface valence states (XPS, JPS-9010 TR Photo-electron Spectrometer, Japan).

Electrochemical measurements

All electrochemical tests of the catalysts were carried out using a Bio-logic VMP3 electrochemical workstation and a standard three-electrode cell configuration in 1.0 M KOH, where the catalyst served as the working electrode, the graphite plate served as the auxiliary electrode, and the saturated calomel electrode (SCE) served as the reference electrode, respectively. The catalysts were electrochemically activated underwent five cycles of cyclic voltammetry (CV) at a scanning rate of 5 mV s^{-1} to reach a stable state. Linear sweep voltammetry (LSV) measurement was conducted to obtain the polarization curves at a scan rate of 0.2 mV s^{-1} for OER performance, respectively. Electrochemical impedance spectroscopy (EIS) was performed with scanning frequency ranging from 200 kHz to 5 mHz. The electrochemically active surface area (ECSA) computation of (C_{dl}) values based on double-layer capacitance was assessed using cyclic voltammetry (CV) at various scan rates. Chronoamperometry was used to evaluate the catalyst's durability and long-term stability. The following CV was run at a scan rate of 5 mV s^{-1}, and the thermodynamic potential of 1.0 M

KOH that had been H_2-saturated for roughly 10 min was determined as the average of the two potentials at the present zero-crossing (1.040 V) in Fig. S1. Moreover, all electrochemical measurements were carried out at room temperature (25±1 °C), and all curves described in this work have been calibrated by *iR* compensation.

Calculation of the active site density and TOF:

The number of active sites (n) of CoP-$Ce_2(CO_3)_2O$/NF was calculated by the TOF value, where we assumed that both Co and Ce species are active sites of CoP-$Ce_2(CO_3)_2O$/NF, and then according to ICP-MS test results (Table S1) calculated the total amount of Co and Ce (molar content: n). The TOFs (s^{-1}) can be calculated by the following equation[1]:

$$TOF = \frac{jA}{2nF} \qquad (1)$$

where *j* is the current density (A cm^{-2}) recorded during the linear sweep voltammetry measurement at certain overpotential, *A* is the geometric surface area of the catalytic electrode, *F* is the Faraday constant (C mol^{-1}), and *n* is the number of active sites (mol) present in the electrode. The 2 present in the equation is due to the two electrons necessary for the formation of one hydrogen molecule starting from two protons ($2H^+ + 2e^- \rightarrow H_2$). Similarly, the electron transfer number is 4 for OER.

Electrochemically active surface areas (ECSA):

The catalyst's real surface area is calculated from the electrochemically active surface area (ECSA), which is obtained from specific capacitance. The normal specific capacitance of flat surfaces ranges from 20–60 μF cm^{-2}_{geo}.

$$A_{ECSA} = \frac{specific\ capacitance}{60\ \mu F\ cm^{-2}_{geo}\ per\ cm^{-2}_{ECSA}}$$

ECSA can be calculated for CoP-$Ce_2(CO_3)_2O$/NF, $Ce_2(CO_3)_2O$/NF, CoP/NF.

$$A_{ECSA}(CoP - Ce_2(CO_3)_2O/NF) = \frac{37.0\ mF\ cm^{-2}}{60\ \mu F\ cm^{-2}_{geo}\ per\ cm^{-2}_{ECSA}} = 616.7\ cm^2_{ECSA}$$

$$A_{ECSA}(Ce_2(CO_3)_2O/NF) = \frac{11.3\ mF\ cm^{-2}}{60\ \mu F\ cm^{-2}_{geo}\ per\ cm^{-2}_{ECSA}} = 188.3\ cm^2_{ECSA}$$

$$A_{ECSA}(CoP/NF) = \frac{10.9\ mF\ cm^{-2}}{60\ \mu F\ cm^{-2}_{geo}\ per\ cm^{-2}_{ECSA}} = 181.7\ cm^2_{ECSA}$$

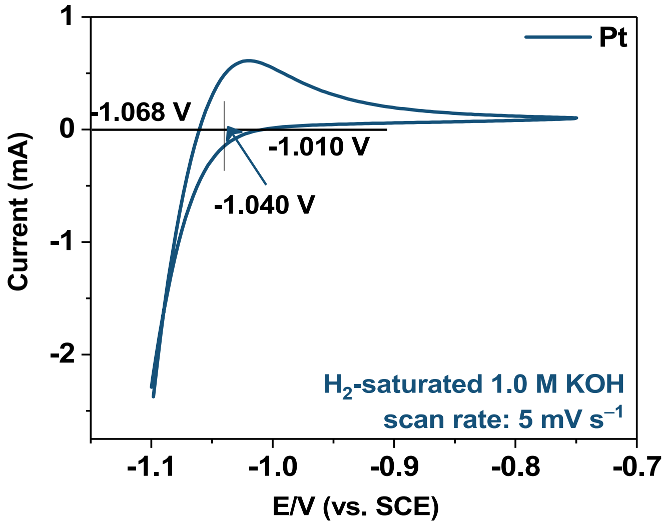

Fig. S1. RHE voltage calibration in 1.0 M KOH.

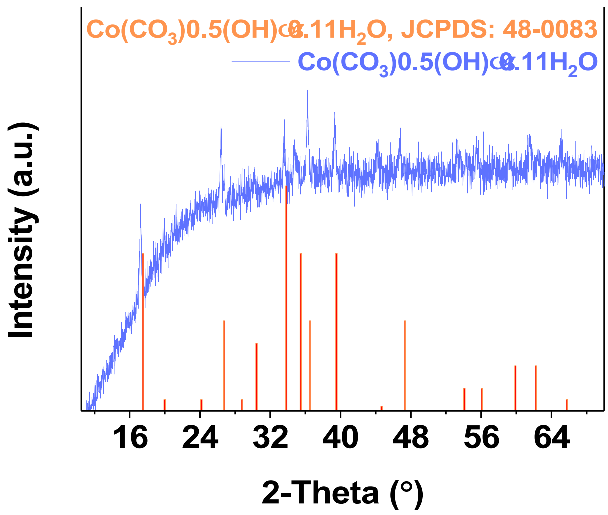

Fig. S2. XRD pattern before phosphorylation of Co precursor.

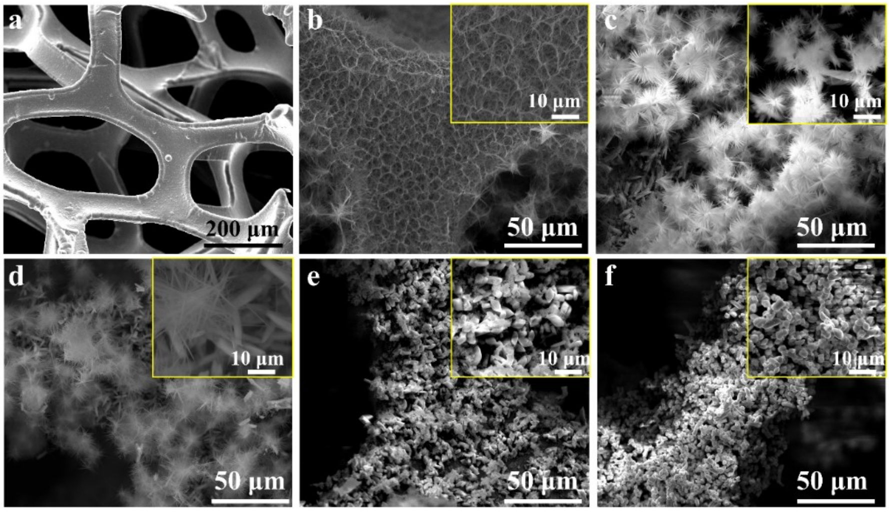

Fig. S3. SEM image of (a) pure nickel foam (NF). SEM images of different Ce/Co ratio precursors before phosphorylation: (b) 0:4, (c) 1:3, (d) 2:2, (e) 3:1, and (f) 4:0.

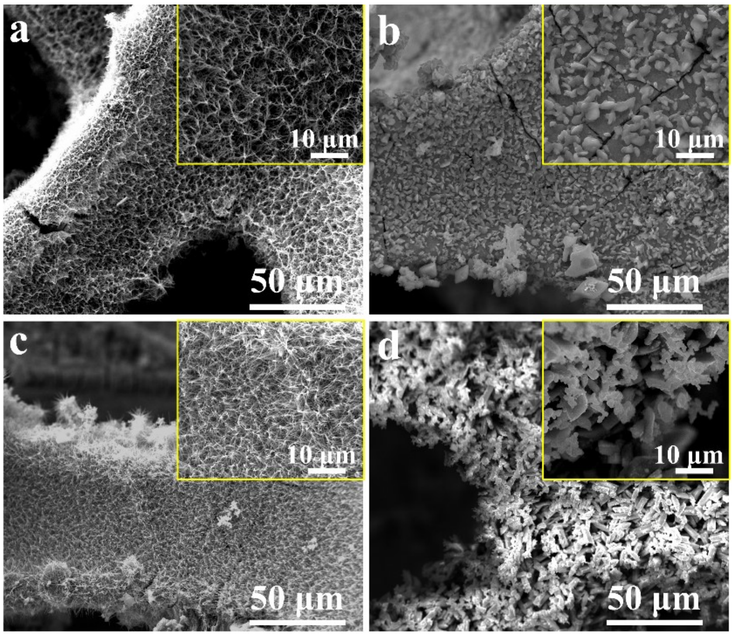

Fig. S4. SEM images of different Ce/Co ratios after phosphorylation: (a) 0/4, (b) 1/3, (c) 2/2, and (d) 4/0.

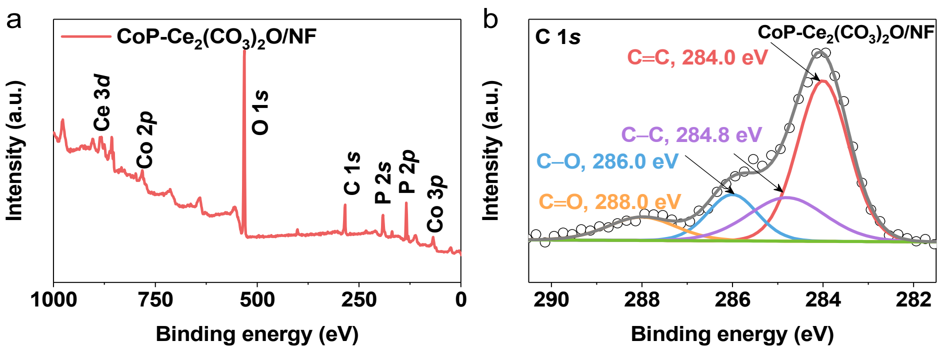

Fig. S5. (a) Full-range XPS survey of CoP-$Ce_2(CO_3)_2O$/NF. (b) High-resolution C 1*s* XPS spectrum of CoP-$Ce_2(CO_3)_2O$/NF.

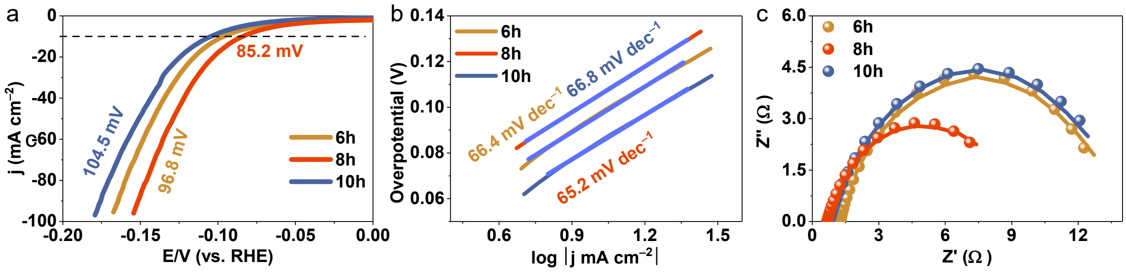

Fig. S6. HER performance of the prepared CoP-$Ce_2(CO_3)_2O$/NF catalysts at different hydrothermal reaction time (6, 8 and 10 h) in 1.0 M KOH. (a) LSV polarization curves, (b) corresponding Tafel slopes, (c) corresponding electrochemical impedance spectroscopy (EIS), and (d) double layer capacitance (C_{dl}).

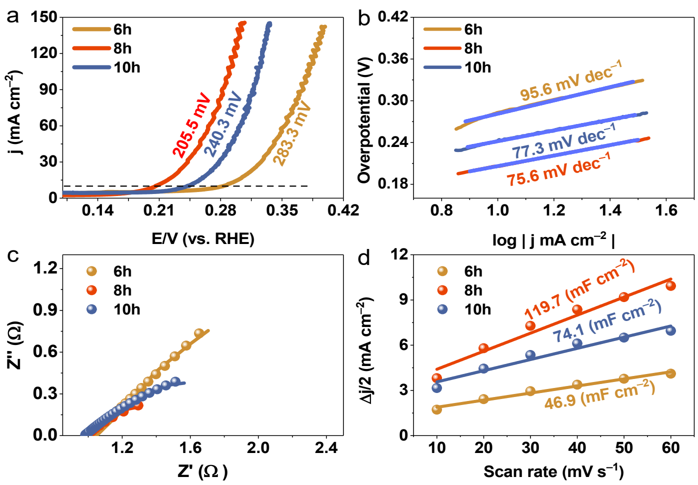

Fig. S7. OER performance of the prepared CoP-$Ce_2(CO_3)_2O$/NF catalysts at different hydrothermal reaction time (6, 8 and 10 h) in 1.0 M KOH. (a) LSV polarization curves, (b) corresponding Tafel slopes, (c) corresponding electrochemical impedance spectroscopy (EIS), and (d) double layer capacitance (C_{dl}).

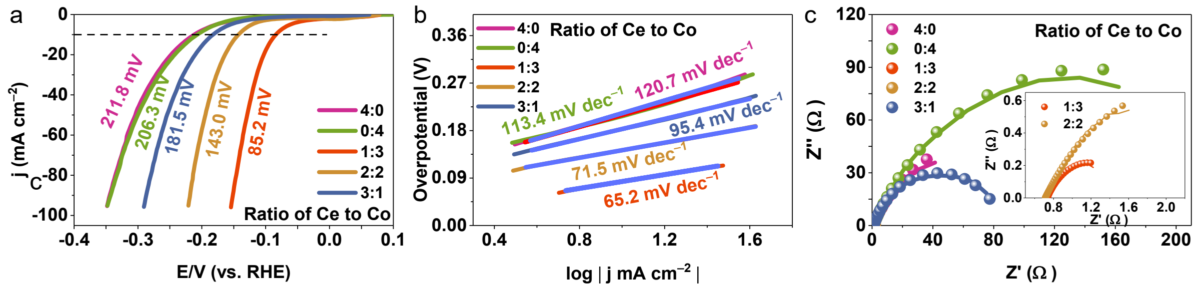

Fig. S8. HER performance of the prepared CoP-$Ce_2(CO_3)_2O$/NF catalysts at different Ce/Co ratios (4/0, 0/4, 1/3, 2/2, 3/1) in 1.0 M KOH. (a) LSV polarization curves, (b) corresponding Tafel slopes, (c) corresponding electrochemical impedance spectroscopy (EIS), and (d) double layer capacitance (C_{dl}).

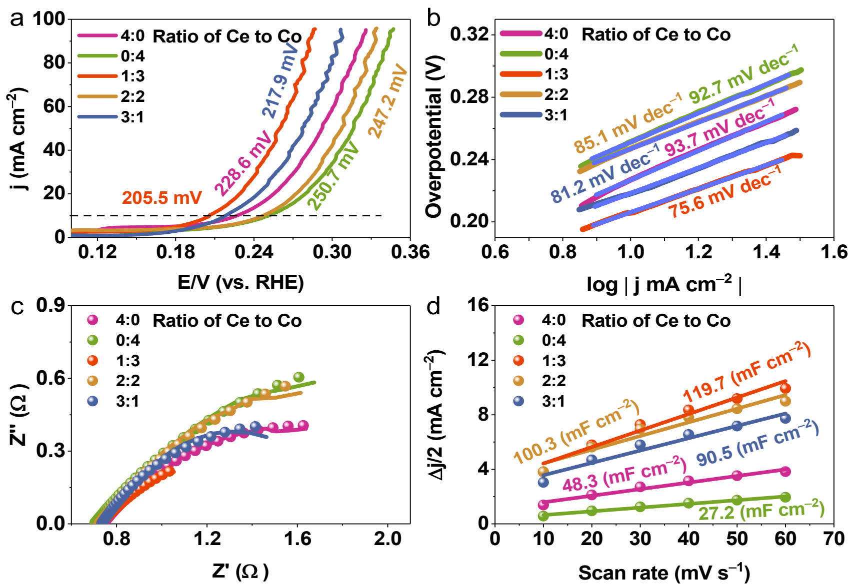

Fig. S9. OER performance of the prepared CoP-$Ce_2(CO_3)_2O$/NF catalysts at different Ce/Co ratios (4/0, 0/4, 1/3, 2/2, 3/1) in 1.0 M KOH. (a) LSV polarization curves, (b) corresponding Tafel slopes, (c) corresponding electrochemical impedance spectroscopy (EIS), and (d) double layer capacitance (C_{dl}).

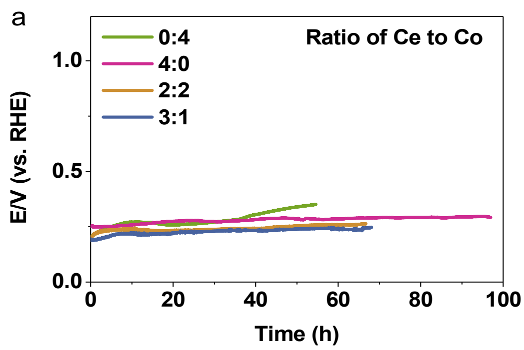

Fig. S10. Stability of the prepared catalysts CoP-$Ce_2(CO_3)_2O$/NF at different Ce/Co ratios (4/0, 0/4, 2/2, 3/1) in 1.0 M KOH for (a) OER, and (b) HER.

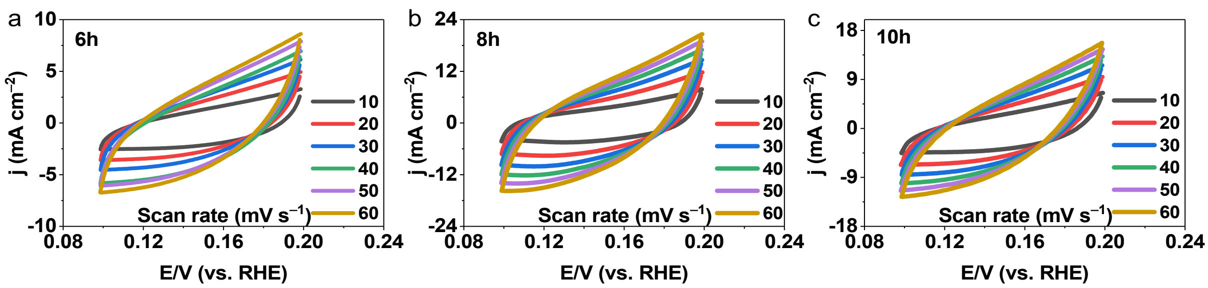

Fig. S11. CV with different scan rates of different hydrothermal reaction time (6, 8 and 10 h) in a non-Faraday potential range of CoP-$Ce_2(CO_3)_2O$/NF.

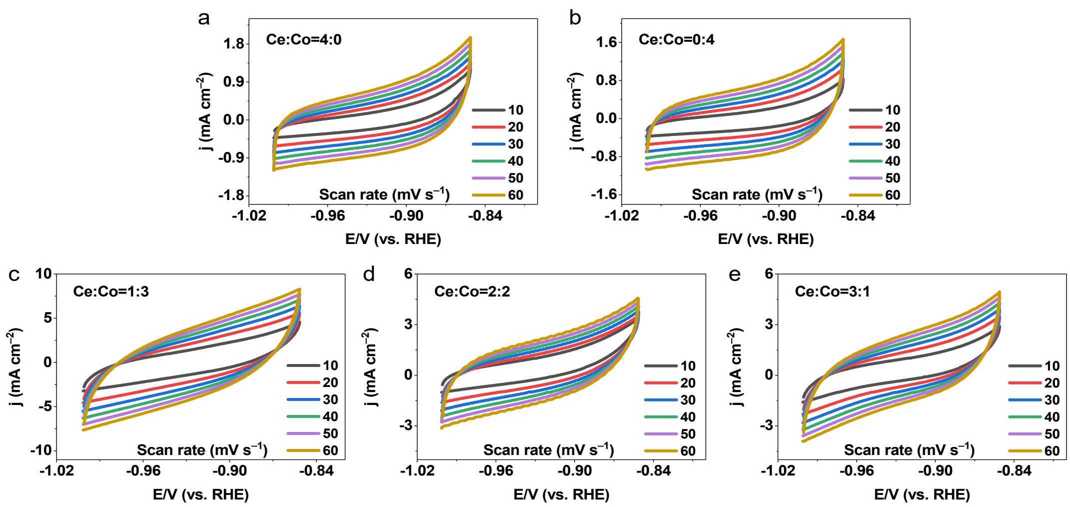

Fig. S12. CV with different scan rates tested in a non-Faradaic potential range in 1.0 M KOH of CoP-$Ce_2(CO_3)_2O$/NF at different Ce/Co ratios: (a) 4/0, (b) 0/4, (c) 1/3, (d) 2/2, and (e) 3/1.

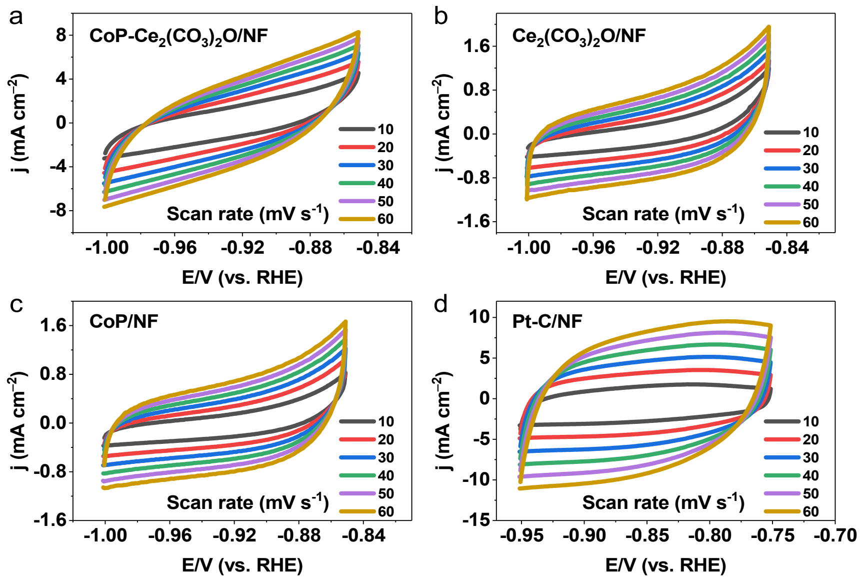

Fig. S13. CV with different scan rates tested in a non-Faradaic potential range in 1.0 M KOH of (a) CoP-$Ce_2(CO_3)_2O$/NF, (b) $Ce_2(CO_3)_2O$/NF, (c) CoP/NF, and (d) Pt-C/NF.

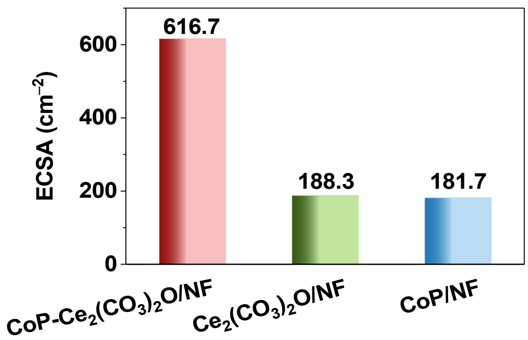

Fig. S14. Electrochemical active surface area (ECSA) of prepared catalysts of CoP-$Ce_2(CO_3)_2O$/NF, $Ce_2(CO_3)_2O$/NF, and CoP/NF.

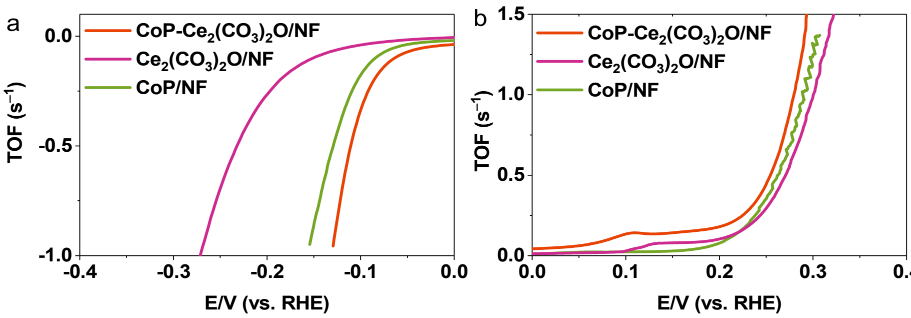

Fig. S15. Turnover frequency (TOF) values of CoP-$Ce_2(CO_3)_2O$/NF, $Ce_2(CO_3)_2O$/NF, and CoP/NF for (a) HER, and (b) OER.

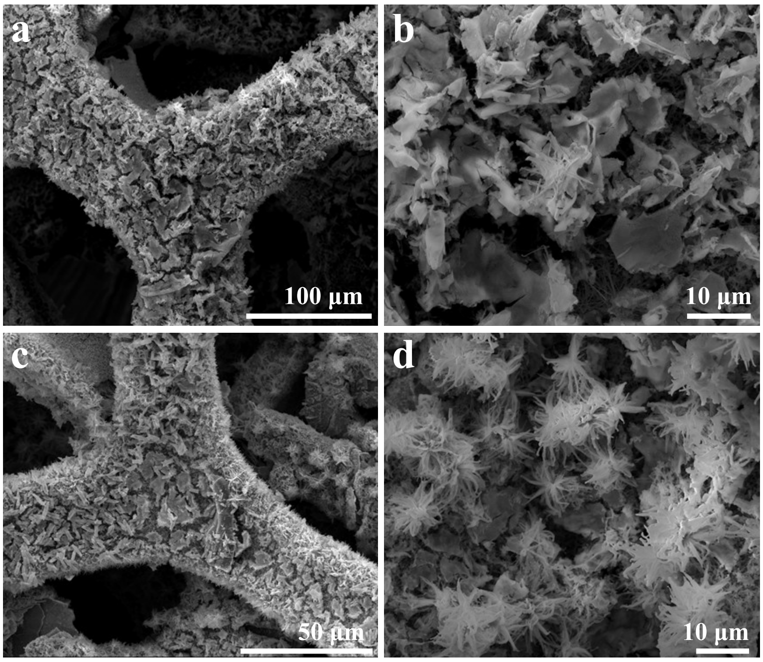

Fig. S16. SEM images of CoP-$Ce_2(CO_3)_2O$/NF catalyst (a-b) after OER stability test, and (c-d) after OER stability test.

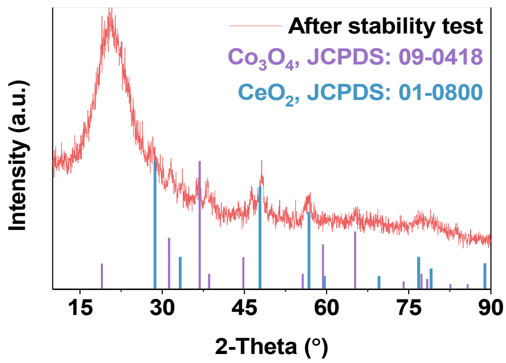

Fig. S17. XRD patterns of CoP-$Ce_2(CO_3)_2O$/NF catalyst after OER stability test.

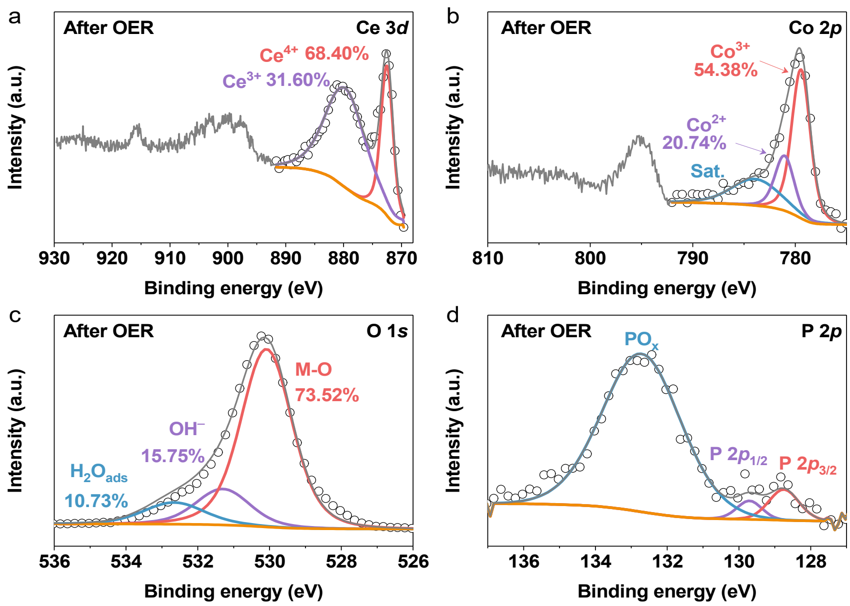

Fig. S18. High-resolution XPS spectra of (a) Ce 3*d*, (b) Co 2*p*, (b) O 1*s*, and (d) P 2*p* for CoP-$Ce_2(CO_3)_2O$/NF after OER stability test.

Table S1. Inductively coupled plasma mass spectrometry (ICP-MS) test results of CoP-$Ce_2(CO_3)_2O$/NF, $Ce_2(CO_3)_2O$/NF and CoP/NF.

Sample	Co (wt %)	Ce (wt %)
4:0	17.90%	N/A
3:1	13.02%	9.61%
0:4	N/A	58.37%

Note: Firstly, the masses of NF and CoP-$Ce_2(CO_3)_2O$/NF with different Co/Ce ratios are weighed, respectively. The difference between them is the quality of the CoP-$Ce_2(CO_3)_2O$/NF loaded on the NF. Subsequently, the catalyst was dissolved in 8 mL of aqua regia, followed by taking 10 μL solution with a pipette and diluted to 100 mL in a volumetric flask. Finally, the concentrations of Co and Ce were tested by ICP-MS. Give an example to this, we first weighed a piece of NF with a mass of 31.13 mg, and the mass after loading CoP-$Ce_2(CO_3)_2O$/NF was 40.65 mg, therefor the mass of the loaded CoP-$Ce_2(CO_3)_2O$ composite was 9.52 mg. Therefore, the total mass concentration of the real composite is: 9.52 mg/8 mL×10 μL/0.1 L = 119 (μg L^{-1}). The ICP-MS test results show that the concentration of Co is 15.488 μg L^{-1}, and the concentration of Ce is 11.432 μg L^{-1}, so the mass fraction of Co is 15.488/119×100%=13.02%, and the mass fraction of Ce is 11.432/119×100%=9.61%.

Table S2. Summary of previously reported excellent HER catalysts in alkaline solution.

Catalyst	η_{10} (mV)	Tafel slop (mV dec^{-1})	Reference
$CoP\text{-}Ce_2(CO_3)_2O/NF$	**85.2**	**65.2**	**This work**
$WCoSe/WCo_3O_4$	98	72	2
$NCO@RuO_2$-NCs	90	54.9	3
$Ni_2P/WS_2/Co_9S_8@C$	67	85.4	4
$ZnCo_2S_4/CoZn_{13}$	160	61.42	5
SW-CoS@CNT	105	51	6
NiYCe-MOF/NF	136	74	7
Mo-NiS_x@NiFe-LDH/NF	61.3	42.3	8
Fe_2P–CoP/CeO_2-20	45	47.6	9
$Ni_{2+x}Fe_{2-x}N$/NC NPNCs	101	86	10
Cu_8S_5/NSC-900	137	136.8	11
NMCP@NF	88	70	12
0.5Ni-1T-MoS_2	112	52.7	13
Chestnut burr-A	105	55	14
V-Ni_3FeN/Ni@N-GTs	66	88	15

Table S3. Summary of previously reported excellent OER catalysts in alkaline solution.

Catalyst	η_{10} (mV)	Tafel slop (mV dec^{-1})	Reference
$CoP\text{-}Ce_2(CO_3)_2O/NF$	**205.5**	**75.6**	**This work**
$WCoSe/WCo_3O_4$	175	62	**2**
$NCO@RuO_2$-NCs	188	74.3	3
$Ni_2P/WS_2/Co_9S_8@C$	204	54.3	4
W-$NiS_{0.5}Se_{0.5}$	171	41	16
$VCoCO_x$@NF	240	65	17
SW-CoS@CNT	218	78	6
NiYCe-MOF/NF	245	65	7
Mo-NiS_x@NiFe-LDH/NF	224	44.41	8
1T-2H MoS_2/CoS_2	261	85	18
Fe_2P–CoP/CeO_2-20	248	39.8	9
$Ni_{2+x}Fe_{2-x}N$/NC NPNCs	270	43	10
Cu_8S_5/NSC-900	313	66.5	11
NMCP@NF	250	41	12
0.5Ni-1T-MoS_2	224	103.2	13

Table S4. Comparison of the overall-water-splitting activities among various recently reported electrocatalysts tested in 1.0 M KOH.

Catalyst (Cathode)	Catalyst (Anode)	Potential (V) 10 mA cm^{-2}	Reference
CoP-$Ce_2(CO_3)_2O$/NF	**CoP-$Ce_2(CO_3)_2O$/NF**	**1.51**	**This work**
Mo_2C-CoO@N-CNFs	Mo_2C-CoO@N-CNFs	1.56	19
NiYCe-MOF/NF	NiYCe-MOF/NF	1.54	7
Mo-NiS_x@NiFe-LDH/NF	Mo-NiS_x@NiFe-LDH/NF	1.54	8
1T-2H MoS_2/CoS_2	1T-2H MoS_2/CoS_2	1.53	18
Co-NC@Ni_2Fe-LDH	Co-NC@Ni_2Fe-LDH	1.55	20
Fe-Ni_2P@C/NF	Fe-Ni_2P@C/NF	1.55	21
CoP@CoOOH/CP	CoP@CoOOH/CP	1.52	22
Fe_2P–CoP/CeO_2-20	Fe_2P–CoP/CeO_2-20	1.52	9
$Ni_{2+x}Fe_{2-x}N$/NC NPNCs	$Ni_{2+x}Fe_{2-x}N$/NC NPNCs	1.51	10
Cu_8S_5/NSC-900	Cu_8S_5/NSC-900	1.64	11
NMCP@NF	NMCP@NF	1.52	12
0.5Ni-1T-MoS_2	0.5Ni-1T-MoS_2	1.54	13
Chestnut burr-A	Chestnut burr-A	1.51	14
V-Ni_3FeN/Ni@N-GTs	V-Ni_3FeN/Ni@N-GTs	1.55	15

References

1. B. Wang, H. Huang, T. Sun, P. Yan, T. T. Isimjan, J. Tian and X. Yang, Dissolution reconstruction of electron-transfer enhanced hierarchical NiS_x-MoO_2 nanosponges as a promising industrialized hydrogen evolution catalyst beyond Pt/C, *J. Colloid Interf. Sci.*, 2020, **567**, 339-346.
2. R. Balaji, T. T. Nguyen, K. Harish, N. H. Kim and J. H. Lee, Modulating heterointerfaces of tungsten incorporated CoSe/Co_3O_4 as a highly efficient electrocatalyst for overall water splitting, *J. Mater. Chem. A*, 2022, **10**, 3782-3792.
3. Z. Zhang, X. Liu, D. Wang, H. Wan, Y. Zhang, G. Chen, N. Zhang and R. Ma, Ruthenium composited $NiCo_2O_4$ spinel nanocones with oxygen vacancies as a high-efficient bifunctional catalyst for overall water splitting, *Chem. Eng. J.*, 2022, **446**, 137037.
4. F.-C. Pan, H. He, Z.-X. Yang, Q. Zheng, D. Lin and Y. Huo, Rationally designed $Ni_2P/WS_2/Co_9S_8$@C multi-interfacial electrocatalyst for efficient overall water splitting, *Chem. Eng. J.*, 2022, **446**, 136961.
5. D. Zhao, M. Dai, H. Liu, Z. Duan, X. Tan and X. Wu, Bifunctional $ZnCo_2S_4$@$CoZn_{13}$ hybrid electrocatalysts for high efficient overall water splitting, *J. Energy Chem.*, 2022, **69**, 292-300.
6. L. Han, Y. Wu, B. Zhao, W. Meng, D. Zhang, M. Li, R. Pang, Y. Zhang, A. Cao and Y. Shang, Carbon Nanotube-Coupled Seaweed-like Cobalt Sulfide as a Dual-Functional Catalyst for Overall

Water Splitting, *ACS Appl. Mater. Interfaces*, 2022, **14**, 30847-30856.

7. F. Li, M. Jiang, C. Lai, H. Xu, K. Zhang and Z. Jin, Yttrium- and Cerium-Codoped Ultrathin Metal–Organic Framework Nanosheet Arrays for High-Efficiency Electrocatalytic Overall Water Splitting, *Nano Lett.*, 2022, **22**, 7238-7245.
8. Y. Li, H. Guo, Y. Zhang, H. Zhang, J. Zhao and R. Song, Hollow Mo-doped NiS_x nanoarrays decorated with NiFe layered double-hydroxides for efficient and stable overall water splitting, *J. Mater. Chem. A*, 2022, **10**, 18989-18999.
9. X. Ding, J. Yu, W. Huang, D. Chen, W. Lin and Z. Xie, Modulation of the Interfacial Charge Density on Fe_2P–CoP by Coupling CeO_2 for Accelerating Alkaline Electrocatalytic Hydrogen Evolution Reaction and Overall Water Splitting, *Chem. Eng. J.*, 2022, **451**, 138550.
10. C.-F. Li, L.-J. Xie, J.-W. Zhao, L.-F. Gu, H.-B. Tang, L. Zheng and G.-R. Li, Interfacial Fe−O−Ni−O−Fe Bonding Regulates the Active Ni Sites of Ni-MOFs via Iron Doping and Decorating with FeOOH for Super-Efficient Oxygen Evolution, *Angew. Chem. Int. Ed.* , 2022, **61**, e202116934.
11. Y. Zhang, L. Chen, B. Yan, F. Zhang, Y. Shi and X. Guo, Regeneration of textile sludge into Cu_8S_5 decorated N,S self-doped interconnected porous carbon as an advanced bifunctional electrocatalyst for overall water splitting, *Chem. Eng. J.*, 2023, **451**, 138497.
12. M. R. Kandel, U. N. Pan, D. R. Paudel, P. P. Dhakal, N. H. Kim and J. H. Lee, Hybridized bimetallic phosphides of Ni–Mo, Co–Mo, and Co–Ni in a single ultrathin-3D-nanosheets for efficient HER and OER in alkaline media, *Compos. Part B Eng.*, 2022, **239**, 109992.
13. G. Wang, G. Zhang, X. Ke, X. Chen, X. Chen, Y. Wang, G. Huang, J. Dong, S. Chu and M. Sui, Direct Synthesis of Stable 1T-MoS_2 Doped with Ni Single Atoms for Water Splitting in Alkaline Media, *Small*, 2022, **18**, 2107238.
14. H. Liu, Z. Li, J. Hu, Z. Qiu, W. Liu, J. Lu and J. Yin, Self-supported cobalt oxide electrocatalysts with hierarchical chestnut burr-like nanostructure for efficient overall water splitting, *Chem. Eng. J.*, 2022, **435**, 134995.
15. G. Song, S. Luo, Q. Zhou, J. Zou, Y. Lin, L. Wang, G. Li, A. Meng and Z. Li, Doping and heterojunction strategies for constructing V-doped Ni_3FeN/Ni anchored on N-doped graphene tubes as an efficient overall water splitting electrocatalyst, *J. Mater. Chem. A*, 2022, **10**, 18877-18888.
16. Y. Wang, X. Li, M. Zhang, J. Zhang, Z. Chen, X. Zheng, Z. Tian, N. Zhao, X. Han, K. Zaghib, Y. Wang, Y. Deng and W. Hu, Highly Active and Durable Single-Atom Tungsten-Doped $NiS_{0.5}Se_{0.5}$ Nanosheet@$NiS_{0.5}Se_{0.5}$ Nanorod Heterostructures for Water Splitting, *Adv. Mater.*, 2022, **34**, 2107053.
17. A. Meena, P. Thangavel, A. S. Nissimagoudar, A. Narayan Singh, A. Jana, D. Sol Jeong, H. Im and K. S. Kim, Bifunctional oxovanadate doped cobalt carbonate for high-efficient overall water splitting in alkaline-anion-exchange-membrane water-electrolyzer, *Chem. Eng. J.*, 2022, **430**, 132623.
18. P. Chang, T. Wang, Z. Liu, X. Wang, J. Zhang, H. Xiao, L. Guan and J. Tao, Interface-assisted phase transition in MOF-derived MoS_2/CoS_2 heterostructures for highly efficient dual-pH hydrogen evolution and overall water splitting, *J. Mater. Chem. A*, 2022, **10**, 16115-16126.
19. T. Gong, J. Zhang, Y. Liu, L. Hou, J. Deng and C. Yuan, Construction of hetero-phase Mo_2C-CoO@N-CNFs film as a self-supported Bi-functional catalyst towards overall water splitting, *Chem. Eng. J.*, 2023, **451**, 139025.
20. T. Guo, L. Chen, Y. Li and K. Shen, Controllable Synthesis of Ultrathin Defect-Rich LDH

Nanoarrays Coupled with MOF-Derived Co-NC Microarrays for Efficient Overall Water Splitting, *Small*, 2022, **18**, 2107739.

21. H. Bai, D. Chen, Q. Ma, R. Qin, H. Xu, Y. Zhao, J. Chen and S. Mu, Atom Doping Engineering of Transition Metal Phosphides for Hydrogen Evolution Reactions, *Electrochem. Energy Rev.*, 2022, **5**, 24.
22. B. Zhang, J. Shan, W. Wang, P. Tsiakaras and Y. Li, Oxygen Vacancy and Core–Shell Heterojunction Engineering of Anemone-Like CoP@CoOOH Bifunctional Electrocatalyst for Efficient Overall Water Splitting, *Small*, 2022, **18**, 2106012.